Upper mantle slab under Alaska: contribution to anomalous core-phase observations on south-Sandwich to Alaska paths

Final preprint : Published in Physics of the Earth an Planetary Interiors (2020), 299, 106427, doi: https://doi.org/10.1016/j.pepi.2020.106427

Authors: Daniel A. Frost[1]*, Barbara Romanowicz[1,2,3], Steve Roecker[4]

Affiliations:

[1]Earth & Planetary Science, University of California, Berkeley, CA, USA

[2]Institut de Physique du Globe de Paris, Paris, France

[3]College de France, Paris, France

[4]Rensselaer Polytechnic Institute, Troy, NY, USA

*Correspondence to: dafrost@berkeley.edu

Abstract

Observations of travel time anomalies of inner core-sensitive PKPdf seismic body waves, as a function of path orientation with respect to the earth's rotation axis, have been interpreted as evidence of anisotropy in the inner core. Paths from earthquakes in the South Sandwich Islands to stations in Alaska show strongly anomalous travel times, with a large spread that is not compatible with simple models of anisotropy. Here we assess the impact of strong velocity heterogeneity under Alaska on the travel

times, directions of arrival and amplitudes of PKPdf. We use 3D ray-tracing and 2.5D waveform modelling through a new, high-resolution tomography model of the upper mantle beneath Alaska. We find that the structure beneath Alaska, notably the subducting slab, is reflected in the patterns of these PKPdf observations, and this can be replicated by our model. We also find similar patterns in observed teleseismic P waves that can likewise be explained by our slab model. We conclude that at least 2 s of the travel time anomaly often attributed to inner core anisotropy is due to slab effects in the upper mantle beneath Alaska.

Introduction

The observation of directionally dependent travel time anomalies of inner-core sensitive body waves, combined with anomalous splitting of core-sensitive normal modes, have been interpreted as evidence of cylindrical velocity anisotropy within the inner core (IC) (Morelli et al., 1986; Woodhouse et al., 1986). The fast axis of anisotropy is within several degrees of the rotation axis, while the slow direction migrates from in the plane of the equator to within 55° of the rotation axis with increasing depth in the IC (e.g. Ishii and Dziewonski, 2002; Lythgoe *et al.*, 2014; Frost and Romanowicz, 2019). This anisotropy has been interpreted as resulting from preferred alignment of anisotropic iron crystals within the inner core (Stixrude and Cohen, 1995). The magnitude of anisotropy has been shown to vary between 0 and 8%, dependent on depth of sampling (e.g. Vinnik et al., 1994; Lythgoe *et al.*, 2014). Meanwhile, its dependence on the longitude of sampling has been interpreted as evidence of a hemispherical dichotomy, where the quasi-western hemisphere shows

48 stronger anisotropy of around 4% in most models, while the quasi-eastern
49 hemisphere show weaker anisotropy of 1-2% (Creager, 1999; Irving and Deuss, 2011;
50 Tanaka and Hamaguchi, 1997)
51
52 Inner core anisotropy is investigated using the core-sensitive body wave, PKP, which
53 comprises two branches sensitive only to the outer core, PKPbc and PKPab, and one
54 branch sensitive to both the outer and inner cores, PKPdf. The PKPab and PKPbc
55 branches are often used as references, in order to reduce the influence of source and
56 origin time errors, as well as upper mantle velocity heterogeneity, on the recorded
57 differential travel times. Residual travel times of PKPdf relative to a 1D reference
58 model show a dependence on the angle of the inner core portion of the ray relative to
59 the rotation axis, ξ (Morelli et al., 1986). Rays with ξ<35° are referred to as polar and
60 are roughly aligned with the fast axis of anisotropy. These rays show negative PKPdf
61 travel time anomalies of up to 10 seconds (Morelli, Dziewonski and Woodhouse,
62 1986; Shearer, 1994; Su and Dziewonski, 1995; Li and Cormier, 2002; Cao and
63 Romanowicz, 2007; Lythgoe *et al.*, 2014; Romanowicz *et al.*, 2015, Frost et al., *in*
64 *revision*). Here, we use observed PKPdf travel times measured relative to predictions
65 from a 1D reference model, referred to as absolute PKPdf travel time anomalies.
66
67 Resolution of the global pattern of inner core anisotropy is limited by spatially
68 heterogeneous sampling of the IC on polar paths. Previous studies have noted the
69 strongly anomalous character of travel times on polar paths from sources in the South
70 Sandwich Islands (SSI) to stations Alaska, where rays with a range in ξ of only 6°

(26<ξ<32°) show a range of 6 s in travel time anomaly, in contrast with ~3 s for the global data in the same ξ range, (Romanowicz et al., 2003; Garcia et al., 2006; Leykam et al., 2010; Tkalčić, 2010; Tkalčić *et al.*, 2015; Frost and Romanowicz, 2017). This behaviour is seen for both PKPdf absolute and PKPbc-df and PKPab-df relative travel times (Supplementary Figure 1). This SSI-Alaska path may also show variations in the amplitude of PKPdf (Long et al., 2018). The SSI-Alaska anomaly has led to complications in the interpretation of inner core structure (Tkalčić, 2010).

Notably, given the frequent seismicity in the SSI, data from this source region to stations in Alaska are often over-represented in catalogues of IC travel time anomalies (e.g. Tkalčić et al., 2002). Previous studies have attempted to explain the discrepant SSI-Alaska PKP data by invoking regional variations in the strength of IC anisotropy (Tkalčić, 2010). Other studies have argued for a source outside of the IC, specifically velocity anomalies in the tangent cylinder of the outer core (Romanowicz et al., 2003), or polar caps with higher concentration of light elements (Romanowicz and Bréger, 2000).

Other explanations have invoked the effect of lower mantle structure where the paths of PKPdf and outer core reference phases PKPbc and PKPab most diverge. Tkalčić et al. (2002) showed that fitting the SSI-Alaska anomaly requires rapid lateral variations in the D′′ layer. Recently, Long et al. (2018) proposed a model with a 3% velocity increase in the lowermost mantle under Alaska, in addition to uniform inner core anisotropy, to explain the SSI-Alaska anomaly. However, to explain the entire pattern

of travel time and amplitude anomalies with lower mantle structure alone requires a rather extreme distribution of heterogeneity near the CMB. Accounting for trade-offs requires either a thickness up to 650 km with a velocity perturbation of +3%, or P velocity increases of 9.75% over a thickness of 200 km, which is far in excess of that seen in tomography: 4 times stronger than that observed in the regional model of Suzuki *et al.*, (2016) and over 10 times stronger than observed in the global model of Simmons et al., (2011). In particular, fitting the variation of the anomaly from the southwest to the northeast across Alaska requires an increasingly thick fast D′′ layer in the lowermost mantle, in contrast with mineral physics considerations which predict that the D′′ discontinuity height decreases towards the northeast (Sun et al., 2016). Moreover, while PcP-P travel time measurements do indicate higher than average wavespeeds in the lower mantle beneath Alaska, the models of Long et al., (2018) predict PcP-P travel time anomalies 3 times greater than observed (Ventosa and Romanowicz, 2015). Thus, while models of D′′ heterogeneity can explain the SSI-Alaska anomaly, the parameters required are hard to reconcile with independent observations. On the other hand, Helffrich and Sacks (1994) suggested that upper mantle structure could be responsible for some portion of PKP travel time anomalies. Indeed, in addition to lower mantle heterogeneity, global tomographic models show strong velocity heterogeneity in the upper 1000 km of the mantle in the vicinity of subduction zones (e.g. Fukao and Obayashi, 2013), resulting from active tectonic processes near the surface.

Here we investigate the source of the SSI-Alaska anomaly, using data from the USArray deployment in Alaska, which offers high spatial resolution of PKPdf travel times. We observe and model the effects of strong upper mantle structure in our recent 3D upper mantle tomography model of Alaska (Roecker et al., 2018) on the direction, slowness and travel time of PKP waves. We show that the complex upper mantle structure under Alaska is likely responsible for much of the SSI-Alaska anomalous PKPdf observations. Observation and modelling of similar behaviour in P waves (that do not sample the core) supports this conclusion.

Upper mantle structure beneath Alaska and 3D effects on PKP propagation

Alaska has been subject to multiple episodes of subduction, collision, and accretion since the mid-Jurassic (Plafker et al., 1994). The present-day subduction of the Pacific plate along the Aleutian arc began at ~55Ma (e.g. Scholl et al., 1986) and manifests as steep subduction in the west, and flat slab subduction in the east, where the Yakutat terrane, an oceanic plateau with a thick, low-density crust, is currently being accreted. The structure of Alaska has been extensively studied using a range of methodologies: receiver functions (e.g. Miller *et al.*, 2018), surface waves (e.g., Feng et al., 2018), arrival time tomography (e.g. Martin-Short et al., 2016), and joint interpretations of body and surface waves (e.g. Jiang *et al.*, 2018). These models show strong and multi-scale velocity heterogeneity throughout the uppermost 800 km of the mantle.

The most recent models take advantage of the newly deployed USArray in Alaska which offers instrumentation with a station spacing of ~85 km. In a separate study,

we obtained a high-resolution model of the upper 400 km of the Alaskan mantle using a joint inversion of regional and teleseismic P and S travel times from 7 months of data in 2017 (Roecker et al., 2018). The main features of this model are (Figure 1): a sharply resolved slab of ~100 km thickness with dVp~ 3%, the Yakutat terrain visible down to 120 km depth with dVp~ -3%, and regions of low velocities on either side of the slab. We note that the slab structure is both stronger and sharper than in previous models (Jiang et al., 2018; Martin-Short et al., 2018, 2016).

Interpretation of PKP travel time anomalies is generally based on the infinite frequency approximation in a 1D mantle, where seismic waves are only affected by velocities along the infinitesimal ray path and where structure only changes with depth. When such corrections for the tomographically resolved structure are applied, they do not fully remove scatter in travel times (Bréger et al., 2000). Moreover, it has been shown that considering the 3D effects of strong velocity heterogeneity on ray paths improves the fit of tomographic models to data (Simmons et al., 2012). Finally, when finite frequency effects are considered, strong heterogeneities, such as a subducting slab, can affect the travel time, waveform, and frequency content of seismic waves that intersect it (Helffrich and Sacks, 1994; Vidale, 1987). Of particular importance for slabs is that the magnitude of the effect is strongly dependent on the incident direction of the wave relative to the dip of the heterogeneity.

Seismic heterogeneity can distort an incident wave front, leading to travel time and directional anomalies. Using an array of multiple stations, the delay time of a wave

across the array, or moveout, can be measured. This moveout is characteristic of the direction from which the wave arrives in terms of direction on the surface, or back-azimuth (θ), and the incidence angle, or slowness (u). The residual of the travel time, slowness, and back-azimuth, relative to a 1D reference model, thus demonstrates the effect that the 3D velocity structure has on the wavefield (e.g. Durand et al., 2018). Using sub-arrays of the USArray (e.g. Ventosa and Romanowicz, 2015), now deployed in Alaska, we can measure the local effects of the structure of the Alaskan mantle.

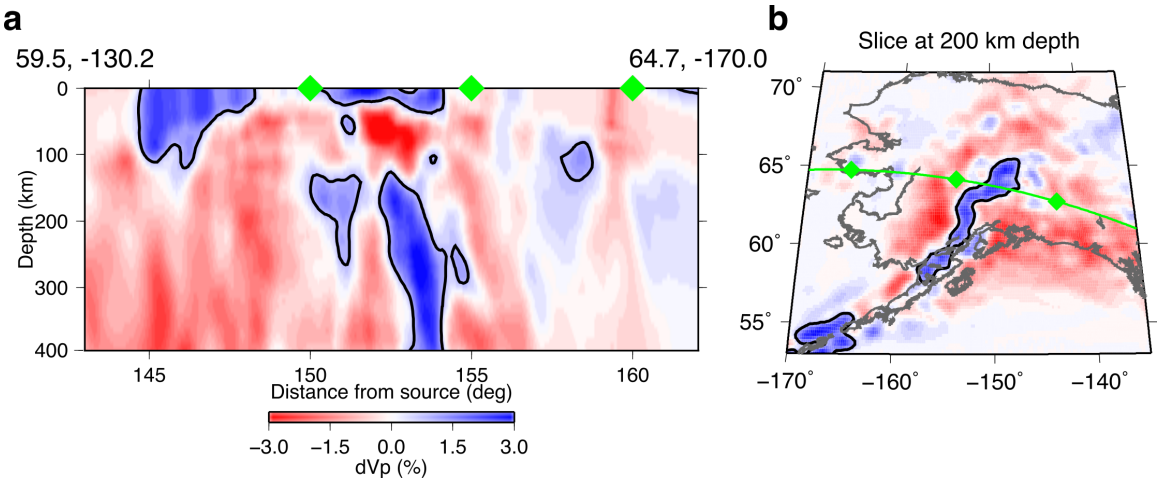

Figure 1: (a) Cross-section of the Vp model of Roecker et al. (2018) along a representative path from event 6 (Suppl. Table 1) to USArray stations displayed as per cent deviation from a 1D reference model. (b) Slice through the model at 200 km depth showing the cross-section path as the green line. Contour marks 0.8% dVp.

Methods

We determine the variation of travel time, slowness, and back-azimuth anomalies across Alaska using a sub-array measurement technique. We use 6 events in the South

Sandwich Islands from 2016 to 2018 (Supplementary table 1) recorded at the USArray and associated networks in Alaska and Canada (AK, AV, CN, II, IM, IU, TA, and US). We collect vertical component seismograms, remove the linear trend and mean from the data, and deconvolve the instrument response. Data are bandpass filtered between 0.4-2.0 Hz, a range which is found to best enhance the clarity of PKPdf relative to the noise.

For each event, we construct sub-arrays of the USArray to measure the travel time, slowness, and back-azimuth of PKPdf at each location. We construct a 1°×1° grid across Alaska, and at each grid point we find the closest station and select an additional 5 to 8 stations around it. Sub-arrays with fewer than 6 stations in total are excluded, and sub-arrays with a non-unique station list are not repeated. The minimum number of stations is chosen to ensure high slowness and back-azimuth resolution. Meanwhile, the maximum number of stations of 9 is chosen to minimise the sampling region of each subarray, thus increasing spatial resolution between subarrays. At each sub-array we window the data 20 s prior to and 40 s after the predicted arrival times of PKPdf and PKPab, respectively according to the 1D reference model ak135 (Kennett et al., 1995). We set the beampoint to the average location of all stations in the subarray. We simultaneously grid search over slownesses from 0 to 8 s/deg, and back-azimuths of ±20° relative to the great-circle path and construct linear stacks, or vespagrams (Davies et al., 1971). We then apply the F-statistic, a coherence measure, which effectively suppresses aliasing, thus sharpening resolution of slowness and back-azimuth (Frost et al., 2013; Selby, 2008).

202 The coherence, F, is computed from the ratio of the sum of the energy in the beam, b,
203 to the summed differences between the beam and each trace used to form the beam,
204 x_i, in a time window, M, normalized by the number of traces in the beam, N :

205 $$F = \frac{N-1}{N} \frac{\sum_{t=1}^{M} b(t)^2}{\sum_{t=1}^{M} \sum_{i=1}^{N} (x_i(t) - b(t))^2} \quad (1)$$

206

207 We visually inspect the F-vespagrams and select the best fitting slowness, back-
208 azimuth, and travel time for PKPdf (Figure 2). We display vespagrams calculated for
209 a range of slownesses (Figure 2c) and back-azimuths (Figure 2d) with the other
210 parameter (back-azimuth and slowness for Figures 2c and 2d, respectively) allowed
211 to vary depending on the maximum F-value. Thus these 2D time-slowness and time-
212 back-azimuth vespagrams effectively display a 3D space. Residual PKPdf travel time
213 and slowness anomalies are measured relative to predictions from ak135, and travel
214 times are corrected for ellipticity (Kennett and Gudmundsson, 1996). Back-azimuth
215 residuals are measured relative to the great-circle path from source to receiver. Sub-
216 arrays for which PKPdf is absent or not clearly resolved are discarded. To improve
217 accuracy of the travel time anomaly measurement, we cross-correlate beams with an
218 empirical PKPdf wavelet. The wavelet is constructed for each event by adaptively
219 stacking (Rawlinson and Kennett, 2004) all selected beams from that event. We then
220 cross correlate each beam with the empirical wavelet and measure the time shift. To
221 account for errors in origin time and source location inherent in using PKPdf absolute
222 measurements, we subtract the median observed travel time from all residual times
223 in the array (corrections are listed in Supplementary Table 1). We correct data for a

model of inner core anisotropy in the upper 450 km of the western hemisphere, constructed without using data from the SSI-Alaska path (model details are given below). This correction accounts for 1.4 to 2.6 s of travel time anomaly, depending on ξ and path length in the inner core. A weaker or stronger anisotropy model would remove less or more of the observed travel time anomaly, respectively.

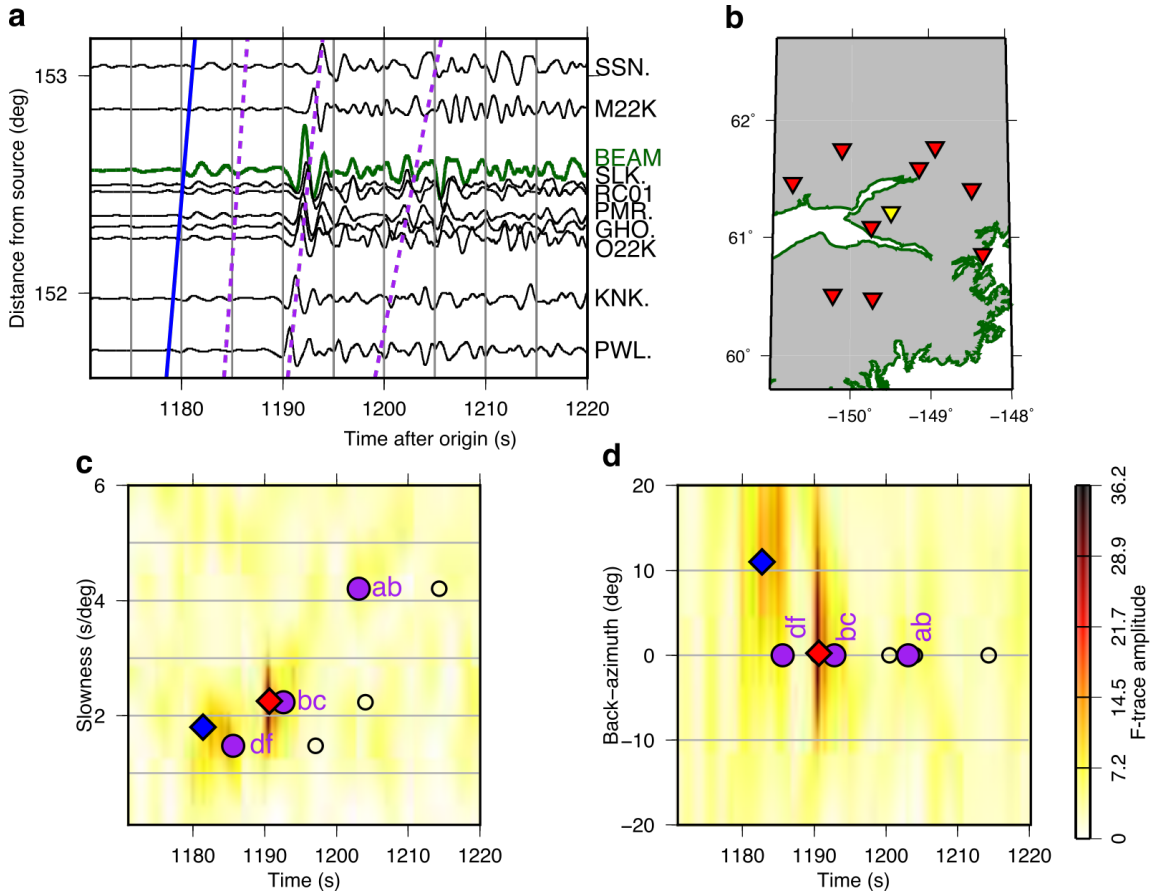

Figure 2: Waveform data, station locations, and resultant F-vespagrams for an example sub-array constructed for event 5 on 2018-08-14 (Suppl. Table 1). (a) PKP wavetrain with PKPdf moveout marked by the blue line, and 1D predictions for PKPdf, PKPbc, and PKPab marked by purple broken lines. Individual stations are shown in

black and the filtered beam is shown in green. (b) Map of stations in the subarray (red) and the beam point (yellow) chosen as the average location of stations in the subarray. F-vespagrams showing time versus (c) slowness and (d) back-azimuth. PKPdf shows a strong back-azimuth anomaly, while PKPbc does not, as is predicted by 3D ray-tracing (Supplementary Figure 2). PKPab appears weak owing to the Hilbert transform, reducing the amplitude and impulsiveness of the phase. The picked PKPdf slowness and back-azimuth is shown by the blue diamond, the maximum F-amplitude, which corresponds to PKPbc, is shown by the red diamond, and predicted arrivals are shown for the direct PKP phases (purple circles) and depth phases (open circles).

The subarray method averages the effects of the structure sampled on all rays used to form the beam to a single location, the beam point. To estimate the minimum spatial resolution of our method we calculate the first Fresnel zone radius for a 1Hz PKP wave at 200 km depth beneath the surface and add this to the aperture of an example subarray. We find that the minimum resolution is thus approximately 220 km, or 2°, and thus we cannot interpret structures smaller than this size, which is about 2 grid points in the regular grids shown in Figures 3.

We use synthetic signals to test the resolution of our method. We simulate signals, combined with real noise at a noise level equivalent to our data, arriving at an example array from a range of incoming directions. We apply the same vespagram and cross-correlation approaches as used with the data and determine our time,

slowness, and back-azimuth resolution to be ±0.1 s, ±1°, and ±0.1 s/deg, respectively. We test the effect of the number of stations in a subarray on beam amplitude and find only a 3% difference between the smallest and largest subarrays. We are thus well able to resolve signals of the magnitude that we observe.

We seek to determine the influence of the Alaskan upper mantle on incoming wave direction and slowness. We forward model PKPdf ray paths through our regional tomographic model of Alaska using a 3D ray-tracer derived from the joint inversion approach described in (Roecker et al., 2010; Comte *et al.*, 2016) and used in the construction of the 3D model (Roecker et al., 2018). In this approach, we compute travel times in the 1D model ak135 from the source up to the edges of the regional tomographic model, and then within the box we apply an eikonal equation solver in a spherical frame (Zhiwei et al., 2009) to find the fastest path through the box to the receiver. We calculate PKPdf travel times through this model and through a simple model, which is 1D throughout. Using the predicted travel times we calculate the incoming direction of the PKPdf wave at the subarrays used in the vespagram process. Unlike the vespagram process where we use waveforms recorded at each station in the subarray, in the ray-tracing process we only have predicted travel times for each station. We select the same stations used in each subarray and fit a plane to the variation of travel time as a function of station location in latitude and longitude, which represents the moveout of the signal. The slope of this surface can be decomposed into a slowness and a back-azimuth. We calculate a single travel time for each subarray as the average of the predicted times for each station. By comparing

predictions of the 3D versus the 1D models we compute the travel time (dT), slowness (du), and back-azimuth (dθ) anomalies resulting from the 3D upper mantle structure.

In order to account for the influence of inner core anisotropy on PKPdf data, we construct a model of inner core western hemisphere anisotropy (167° W and 40° E) using the PKPab-df and PKPbc-df measurements used in Frost and Romanowicz, (2019) and Frost et al. (*in prep*). To construct a model of inner core anisotropy that can be used to correct PKPdf travel times on the SSI-Alaska path, but is not dependent on the SSI-Alaska data, we select only PKPdf data observed at stations outside of Alaska and with PKPdf paths turning less than 450 km below the ICB (which corresponds to the range of depths sampled by SSI-Alaska paths). We attribute the entire PKPdf travel time anomaly to structure in the IC, and convert travel times to velocity anomalies relative to ak135 as: $\frac{dt}{t} = \frac{-dv}{v}$, where t and v are reference travel times and velocities in the IC, respectively, calculated in model ak135. This accounts for the difference in path length between the shallow and more deeply travelling waves. We construct cylindrically symmetric models of anisotropy, in which the perturbation to an spherically symmetric model, after Song (1997), is expressed as:

$$\frac{\delta v}{v_0} = \alpha + \varepsilon \cos^2 \xi + \gamma \sin^2 2\xi \qquad (2)$$

where v and δv represent the reference velocity and velocity perturbations, respectively, and ξ the IC paths make with the rotation axis. By fitting our data with

an L1-norm, we determine the coefficients α, ε, and γ to be: -0.028, 2.626, and -0.996, respectively (Supplementary Figure 1).

Modelling travel time, slowness and back-azimuth anomalies

After correction for inner core anisotropy as described above, the observed PKPdf travel time, slowness, and back-azimuth anomalies show systematic patterns as a function of location across the USArray (Figure 3). We measure travel time residuals of ±1.5 s, slowness residuals of ±0.6 s/deg, and back-azimuth anomalies reaching ±15 deg but more commonly around ±5 deg. The patterns are consistent between events. The most obvious features are:

(1) a trend from late to early arrival from the southeast of Alaska, overlying the Yakutat terrain, towards the northwest

(2) low slownesses in the southeast of Alaska, sharply contrasted by a band of high slownesses trending northeast-southwest across the middle of Alaska

(3) a patch of low back-azimuth residuals in the centre of Alaska, surrounded by high residuals

When viewed in the context of our 3D tomographic model, we find that these sharp contrasts surround the slab (where the slab is defined by >+0.8 % dVp).

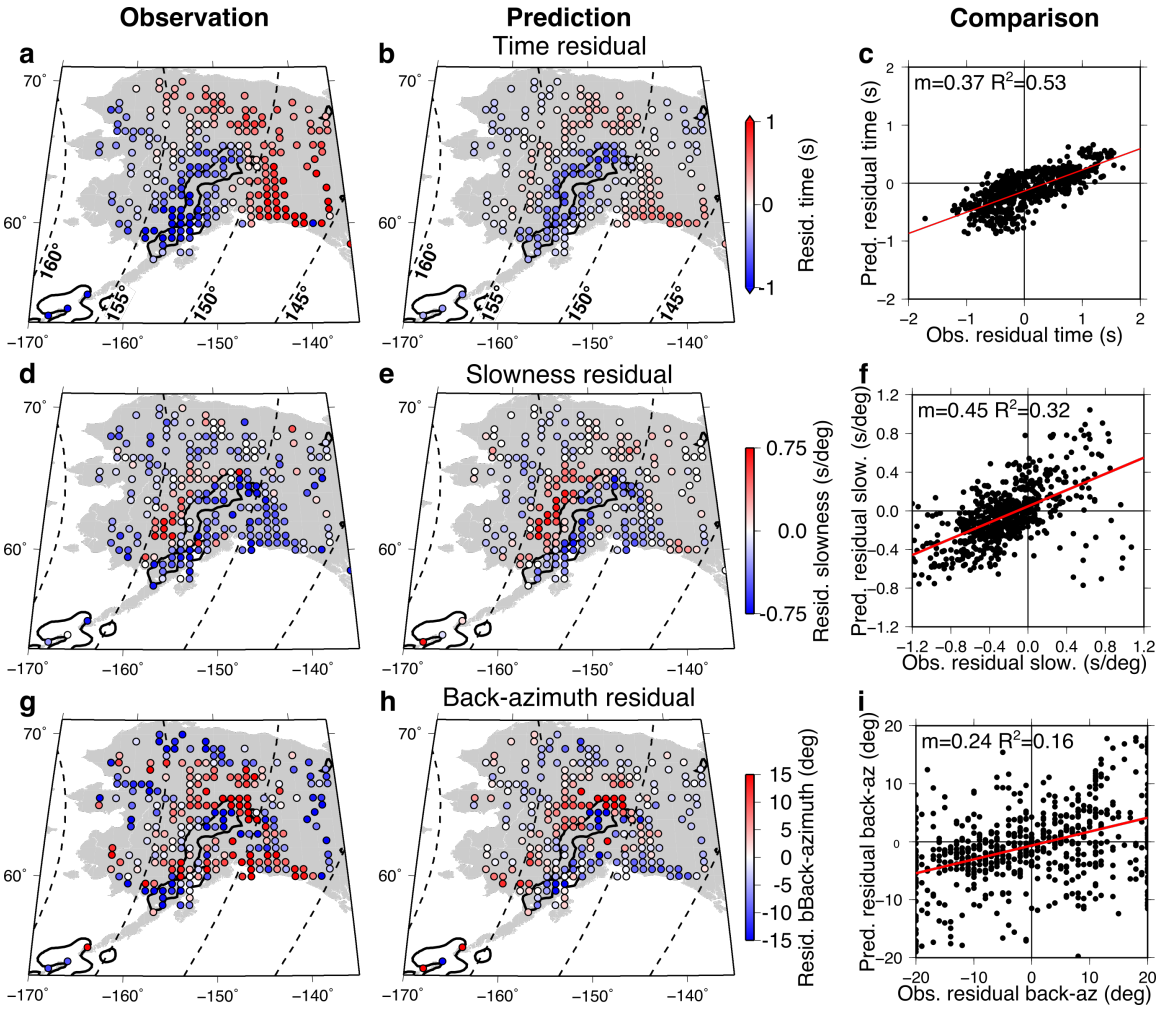

Figure 3: Observed (left), predicted (middle) and comparison (right) of absolute PKPdf ray anomalies from 3D ray-tracing through our preliminary tomography model of Alaska, for all 6 events. (a, b and c): travel time residuals. (d, e, f): slowness residuals; (g, h, i) back-azimuth residuals. The outline of the Alaskan slab at 200 km depth (+0.8% dVp) from the preliminary tomography model is shown in black. The median observed absolute PKPdf travel time is subtracted from each event to account for origin time and location errors.

The corresponding anomalies predicted by 3D ray-tracing through the upper mantle tomography model of Alaska for all events show a striking similarity to the observed travel time, slowness, and back-azimuth anomalies, respectively (Figure 3b, e, and h). The predictions replicate each of the three main features listed above, most strikingly the slowness and back-azimuth anomalies. In addition, the model replicates the trend of increasing and then falling travel time anomaly with distance for rays on azimuths which intersect the slab (Supplementary Figure 3), as observed by Romanowicz et al. (2003) and Long et al. (2018). We see strong agreement of the trends of the observed and predicted anomalies, but a mismatch in the travel time anomaly amplitude, with the predicted anomalies being roughly half of the strength of those observed (Figure 3c, f, and i).

We also predict travel time, slowness, and back-azimuth anomalies for PKPab and PKPbc phases. Predicted differential PKPab-df anomalies range between ±0.4 s, ±0.8 s/deg, and ±30 deg for time, slowness, and back-azimuths respectively, while differential PKPbc-df anomalies range between ±0.1 s, ±0.2 s/deg, and ±15 deg for time, slowness, and back-azimuths respectively. The large variability in back-azimuth anomalies matches our observations (Figure 2), and likely results from the greater sensitivity of back-azimuth on a steeply incident phase (e.g. PKPdf) to small directional changes.

The degree of qualitative agreement between the observations and predictions attests to the important influence of upper mantle heterogeneity on the raypaths and

356 travel times of body waves used to investigate the inner core. Nonetheless, there are
357 discrepancies, which point towards limitations: details and strength of the slab
358 model, unmodelled structure outside of the upper mantle, and potentially the
359 imprecision of the infinite frequency approximation of ray theory. We attempt to
360 improve the fit to the observations by perturbing the slab model and investigate the
361 effect that finite frequency effects may have by waveform modelling.
362
363 The clearest shortcomings of the model are the magnitude of the predicted travel time
364 anomalies, which are less than half of those observed. Tomographic inversions often
365 recover reduced amplitudes of velocity heterogeneity relative to those resolved by
366 forward waveform modelling. The velocity anomaly of the slab as recovered in our
367 model reaches a maximum of around ~3% dVp. We test the effect that stronger
368 heterogeneity may have on the fit by saturating positive velocity anomalies in the slab
369 regions (which we define as all grid points with dVp≥0.8 %) to 4%. We also test the
370 effect of scaling the velocity anomalies in the entire model by factors of 2, 2.5, and 3.
371 We find that the fit between the observed and predicted anomalies improves as we
372 increase the scaling of the tomography model (Supplementary Figure 4 and
373 Supplementary Table 2). This supports our hypothesis that some of the misfit
374 between the observed and predicted times could come from the damping effects of
375 tomographic models. However, the scatter in the predicted measurements also
376 increases, which indicates that the details of the slab model should be improved.
377 Furthermore, the slope of the linear fit between the observed and predicted
378 slownesses and back-azimuths reaches 1 (thus is directly proportional) at scaling

379 factors lower than for the travel times (red text in Suppl. Table 2), thus placing an
380 upper limit on the travel time anomaly that can come from the upper mantle, since
381 attempting to match the observed travel time anomalies by scaling results in over-
382 predicting slowness and back-azimuth anomalies. This suggests either inaccuracy in
383 modelling the incoming ray direction, or that matching the observed travel time
384 anomaly requires heterogeneity outside of the upper mantle. Meanwhile, taking all
385 these factors into consideration, scaling the tomography model by a factor of 2.5
386 works best.
387
388 Predicted azimuth anomalies from our tomography model disagree with the
389 observed back-azimuth in the southeast portion of Alaska. Our model predicts strong
390 negative back-azimuth anomalies while we observe strong positive anomalies
391 (Figure 3g,h). However, the model of Martin-Short et al., (2016) better matches the
392 trend of our observations (Supplementary Figure 5). This discrepancy may arise from
393 lack of resolution of the Yakutat anomaly in our tomography model.
394
395 While our model is only resolved down to 400 km depth, previous tomographic
396 inversions of the Alaskan mantle resolve the slab down to at least 600 km and
397 potentially beyond, although the high velocity anomaly of the slab becomes diffuse
398 towards the bottom of the modelled volume (Martin-Short et al., 2016). Although the
399 model of Martin-Short et al. (2016) covers a smaller region of Alaska than our model
400 and shows weaker heterogeneity by a factor of 1.5, this model images the mantle
401 down to 800 km depth. We use this model to test the influence of the deeper section

of the slab on predicted travel time, slowness, and back-azimuth anomalies. We compute predicted anomalies using the whole 800 km of the model, and using the model cut at 400 km depth to determine the influence of the deeper part of the slab. We find that fit between the predictions and observations is marginally improved when calculated using the 800 km thickness of the model (Supplementary Table 2).

We compare observations and predictions for different scaling factors of the tomographic model along cross sections that are representative of the effects of the Alaskan slab (Supplementary Figure 6). We choose two slices where we observe both negative travel time residuals over the slab, and positive travel time residuals either side of the slab. These azimuth sections (Supplementary Figure 6) allow us to identify the regional variation of misfit between the observations and predictions across Alaska, which either point towards local inaccuracies in the tomography model, or else some other unmodelled structure. Across all of our events, it appears that the current model of Roecker et al., (2018) underrepresents the magnitude of the velocity reduction at shorter distances over the Yakutat (region A in Supplementary Figure 6); this region is better fit when the model is scaled up by a factor of 2. In contrast, the predictions of the current model for the early arrivals caused by the high velocity slab fit the observations (region B in Supplementary Figure 6) at all azimuths except in the far southwest towards the Aleutians. The increasingly negative travel time anomalies at distances >157° are not fully matched in magnitude by any of our models, but are best matched by the standard model (region C in Supplementary Figure 6). Increasing the scaling of the model appears not to improve the fit to travel time anomalies at

425 distance >157°. We produce a hybrid model scaled by a factor of 2.5 before the slab
426 the slab, and 1 over and after the slab. This model generally fits the data better than
427 any other model (Figure 4), although it still fails to fully explain the data at distances
428 beyond 157°. This information will inform future iterations of the Alaskan upper
429 mantle tomography model.
430
431

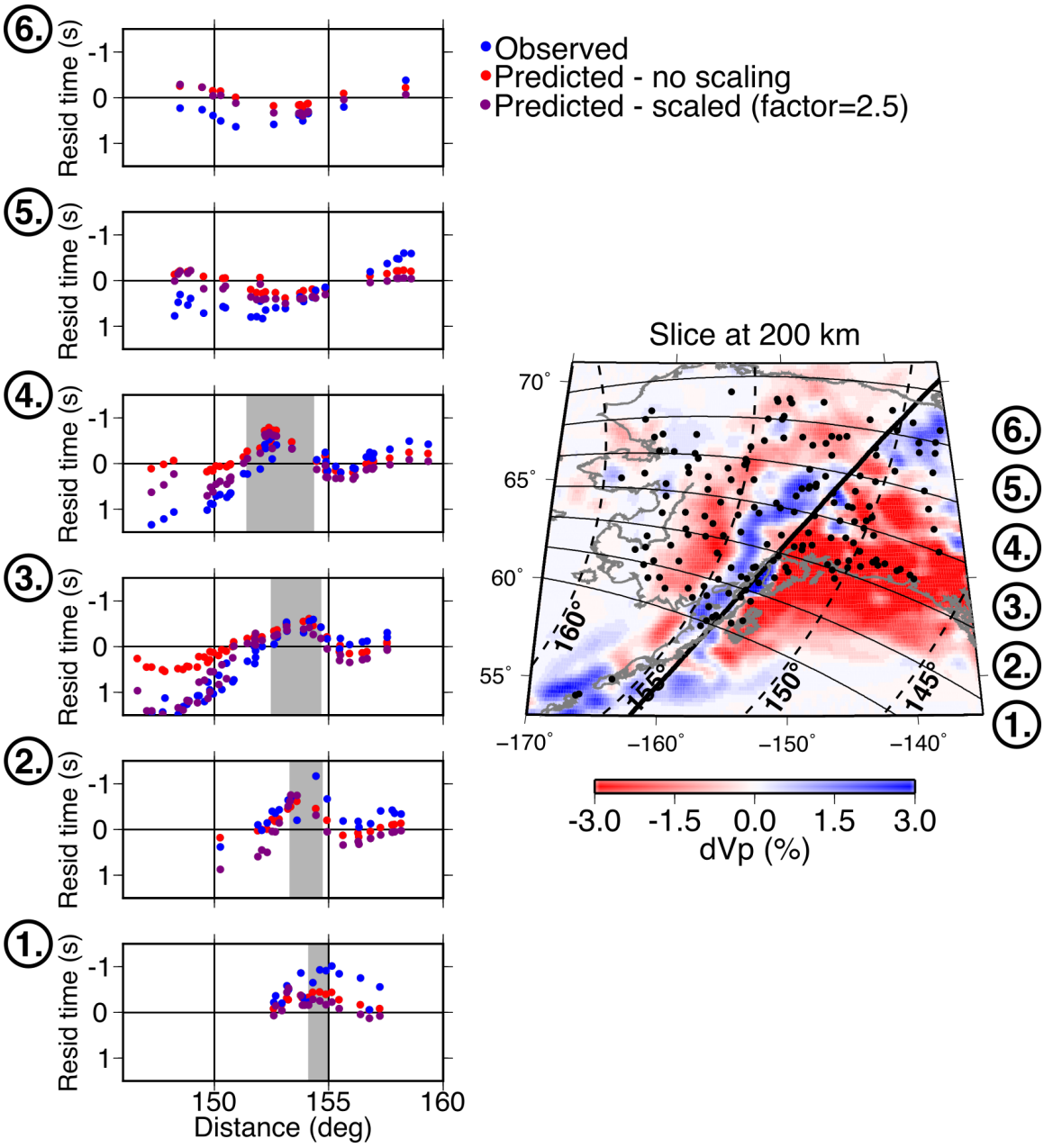

Figure 4: Left: Absolute PKPdf travel time anomalies as a function of distance and for different sections through the slab for event 6 on 2018-12-11. Observations are shown in blue and predictions from 3D ray-tracing through the standard and scaled tomography model (shown on the right) are shown in red and purple, respectively. The rough location of the slab in each cross section is marked by grey shading. The tomography model (right) is scaled by a factor of 2.5 before the slab (south-east of

439 the thick black line) and is kept as standard over and after the slab (north-west of the
440 thick black line). The model is shown at 200 km depth, with stations shown as black
441 circles. Azimuths sections shown on the left are labelled on the right.
442
443 In order to estimate the effect of the slab and surrounding heterogeneity on the travel
444 times and amplitudes of PKPdf, we use axiSEM (Nissen-Meyer et al., 2014) to simulate
445 the effect of the upper mantle on the wavefield. We take a 2D slice through the
446 tomography model (the same as that shown in Figure 1) and calculate waveforms for
447 a regular station spacing of 0.5° at a maximum frequency of 0.5 Hz. We find that this
448 results in both positive and negative PKPdf residual times relative to the 1D
449 prediction of ~1s (Figure 5), which is less than that observed and predicted by the 3D
450 ray-tracing.
451

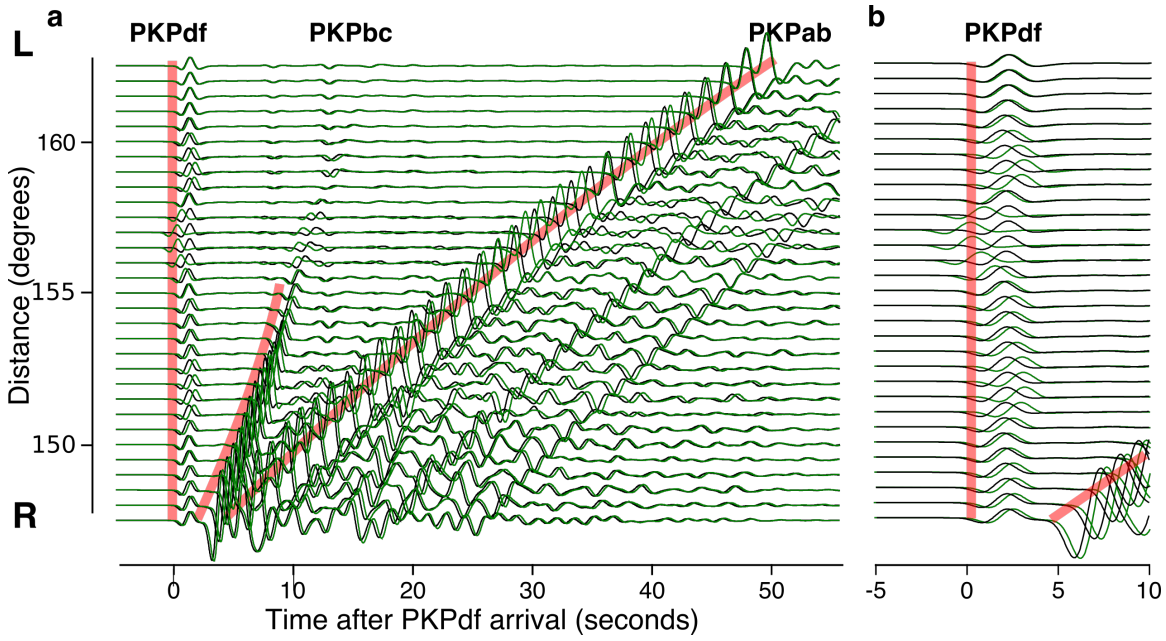

452

Figure 5: 2.5D synthetic PKP waveforms generated for a 1D model (black) and for the cross-section shown in Figure 1 through a saturated version of our 3D model (green), aligned on the predicted arrival time for PKPdf showing (a) the whole PKP wavetrain, and (b) focussing on the PKPdf arrival. The slab model leads to both positive and negative travel time delays of the PKP waves and changes in amplitude, relative to 1D. Synthetics are calculated at 2s maximum period. Predicted arrival times in the 1D model are marked in red.

To further test the robustness of the observed raypath anomalies, we calculate synthetic waveforms through our upper mantle model using a 0.04° station spacing to allow us to simulate high-resolution arrays. For the synthetics, both the subarray spacing and station spacing in each subarray are much higher than in our data, but subarray aperture is approximately the same as in the data. We do this to resolve the effects of the heterogeneity on the waves as accurately as possible but with a similar spatial sensitivity to the data. This is not designed to serve as a test of the slowness resolution of our observations. We use the same vespagram approach as is applied to the data to measure the slowness anomaly that would result from this upper mantle heterogeneity. We find similar patterns of both travel time and slowness anomalies between the synthetics and our observations (Figure 6). We cannot assess back-azimuth anomalies due to the rotationally symmetric nature of the synthetic model. As we see in the 3D raytracing results, the observations of slowness are well fit by the standard model, but the travel times are better fit by a model scaled by a factor of 2. Some discrepancies may result from the simulations being run at a

maximum period of 2 s for sake of computational cost, while we make observations on seismograms with a dominant period of around 1 s.

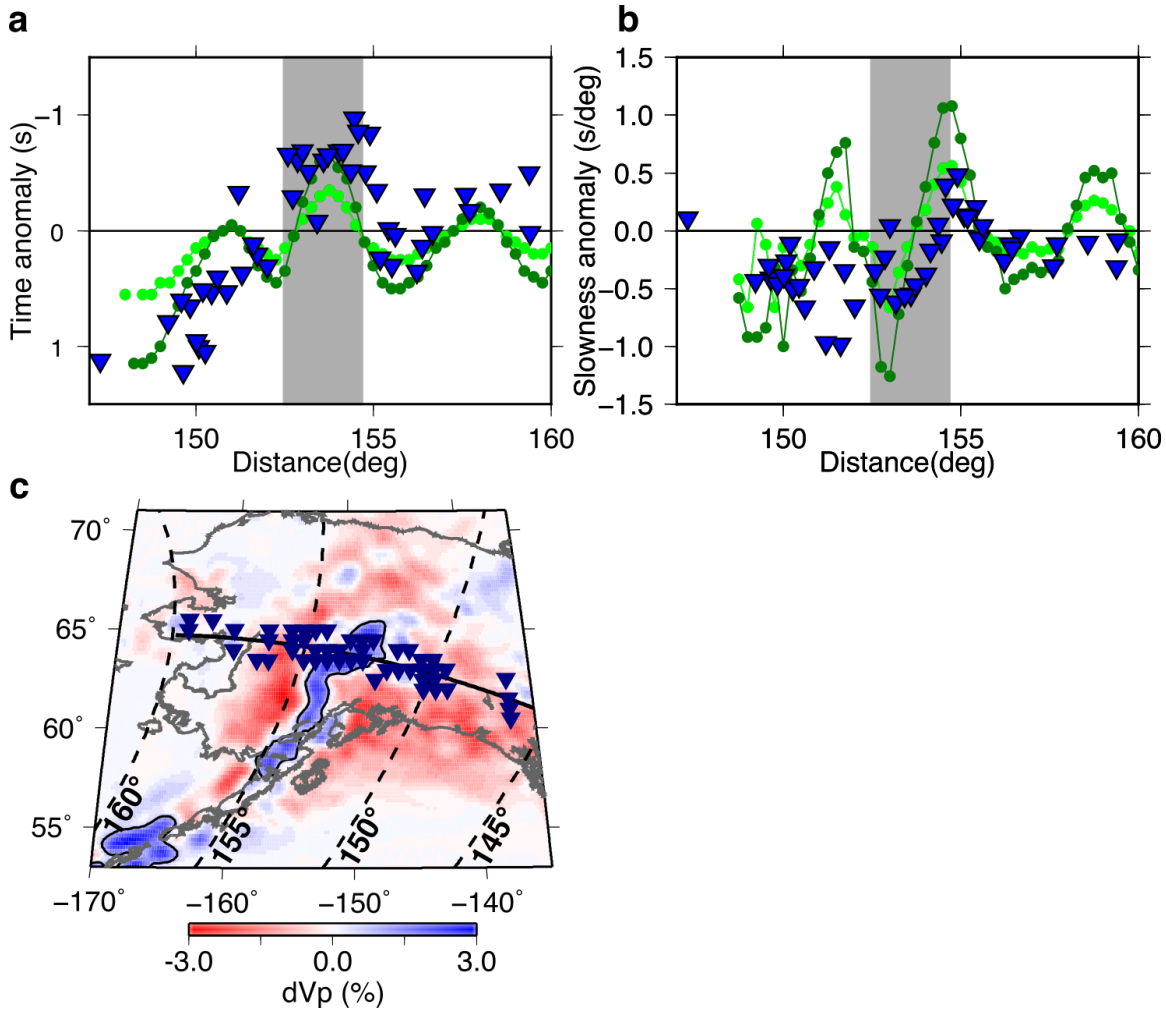

Figure 6: (a) Travel time and (b) slowness anomalies of PKPdf resulting from propagation through the 3D upper mantle model relative to a 1D model. The wavefield is simulated using axiSEM through a 2.5D slice shown in Figure 1. Displayed are synthetics for the standard model (light green), the model scaled by a factor of 2 (dark green) and observations (blue inverted triangles) within 1° of the same profile for all events. (c) Map of the standard upper mantle tomography model at 200 km depth, showing the profile used in the waveform simulation in black, with the

locations of the selected stations shown as blue triangles. The rough location of the slab in the cross-sections is shown by grey shading, and by the black contour on the map.

Modelling PKPdf amplitude variations

Amplitude variations of the PKPdf wave across Alaska measured relative to PKPbc were recently reported by Long et al., (2018) and were attributed to the effects of a high velocity layer in the lowermost mantle. We measure the PKPdf amplitudes at stations across the USArray in Alaska relative to the empirical PKPdf wavelet constructed for each event. We find that PKPdf amplitude decreases over the slab and that this pattern is consistent between events (Figure 7). The range of amplitude ratios observed across Alaska is smaller than seen in amplitude ratios measured on a global scale, which are ascribed to inner core attenuation (Souriau and Romanowicz, 1997), thus we suspect a different cause.

We measure the PKP amplitudes and amplitude ratios predicted by our waveform models. We find that the trend in the predicted PKPdf amplitude matches that in the data, except around ~152°, which corresponds to the edge of the slab (Figure 7). The synthetics predict larger changes in amplitude over a short distance than is observed. This likely results from a combination of: (1) the limitations of the synthetic models, the fact that the calculation is 2.5D and not fully 3D and calculated at only 2 s period and (2) calculating the observed amplitude on beams from sub-arrays. The aperture of our sub-arrays is ~1°, which would smooth out features as sharp as that seen in

the synthetics. We use moving averages of both the data and the synthetics to smooth out the small-scale structure resulting in more similar amplitude patterns (diamonds in Figure 7b).

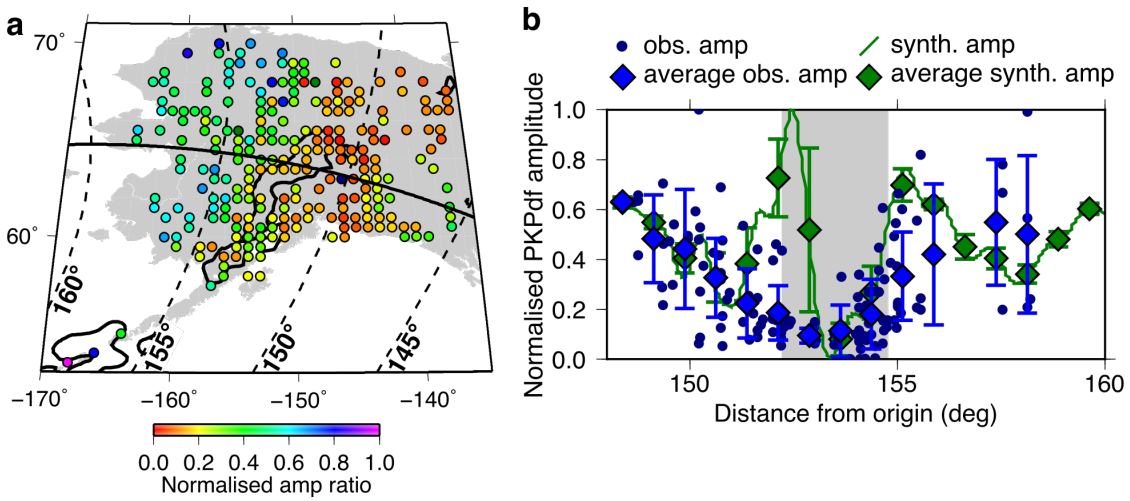

Figure 7: (a) Observed amplitude of PKPdf relative to an empirical wavelet, averaged across all 6 events. Amplitudes are normalised to the maximum in each event before being combined in the average across all events. (b) Observed and synthetic PKPdf amplitudes within ±1° of section marked by black line, which is the section shown in Figure 1. Both observed and synthetic amplitudes are renormalised to the same scale. Moving averages and 1 standard deviation error bars are calculated every 1.5°. The outline of the Alaskan slab at 200 km depth (+0.8% dVp) from the preliminary tomography model is shown in black in (a) and by grey shading in (b).

Discussion

In summary, we find that all of our observations of PKPdf travel time, slowness, back-azimuth, and amplitude variations across Alaska are consistent with the effects of the

526 slab in the Alaskan upper mantle. In particular, the subducted slab causes sharp
527 deviations in wave direction and wave amplitude. Meanwhile, the south-eastern
528 portion of Alaska shows consistently slow travel times, potentially caused by the
529 underlying Yakutat lithosphere. These complexities point to the upper mantle
530 contributing at least 2 s to PKPdf travel time anomalies, which thus should not be
531 attributed to inner core anisotropy.
532
533 To confirm this slab effect, we measured the travel time, slowness, and back-azimuth
534 anomalies from three events from the Caribbean and South America that travel to the
535 USArray in Alaska along similar back-azimuths as PKP paths from SSI, but at distances
536 corresponding to P waves (that do not sample the core). Event details are given in
537 Supplementary Table 3. We applied the same sub-array processing described here
538 for PKP. While direct P waves arrive at higher slownesses than PKP, we find very
539 similar patterns to those observed for PKPdf, and a similarly strong fit between
540 observations and predictions from 3D ray-tracing through an Alaskan tomographic
541 model (Supplementary Figure 7). Notably, the observed patterns as a function of
542 azimuth and distance are better matched by predicted travel times for our
543 unmodified tomographic models than for PKPdf (Figure 8). Because P waves sample
544 the slab at shallower depths than PKPdf, this indicates that improvement in the
545 deeper part of the slab model may be needed, which we will address in a forthcoming
546 study.

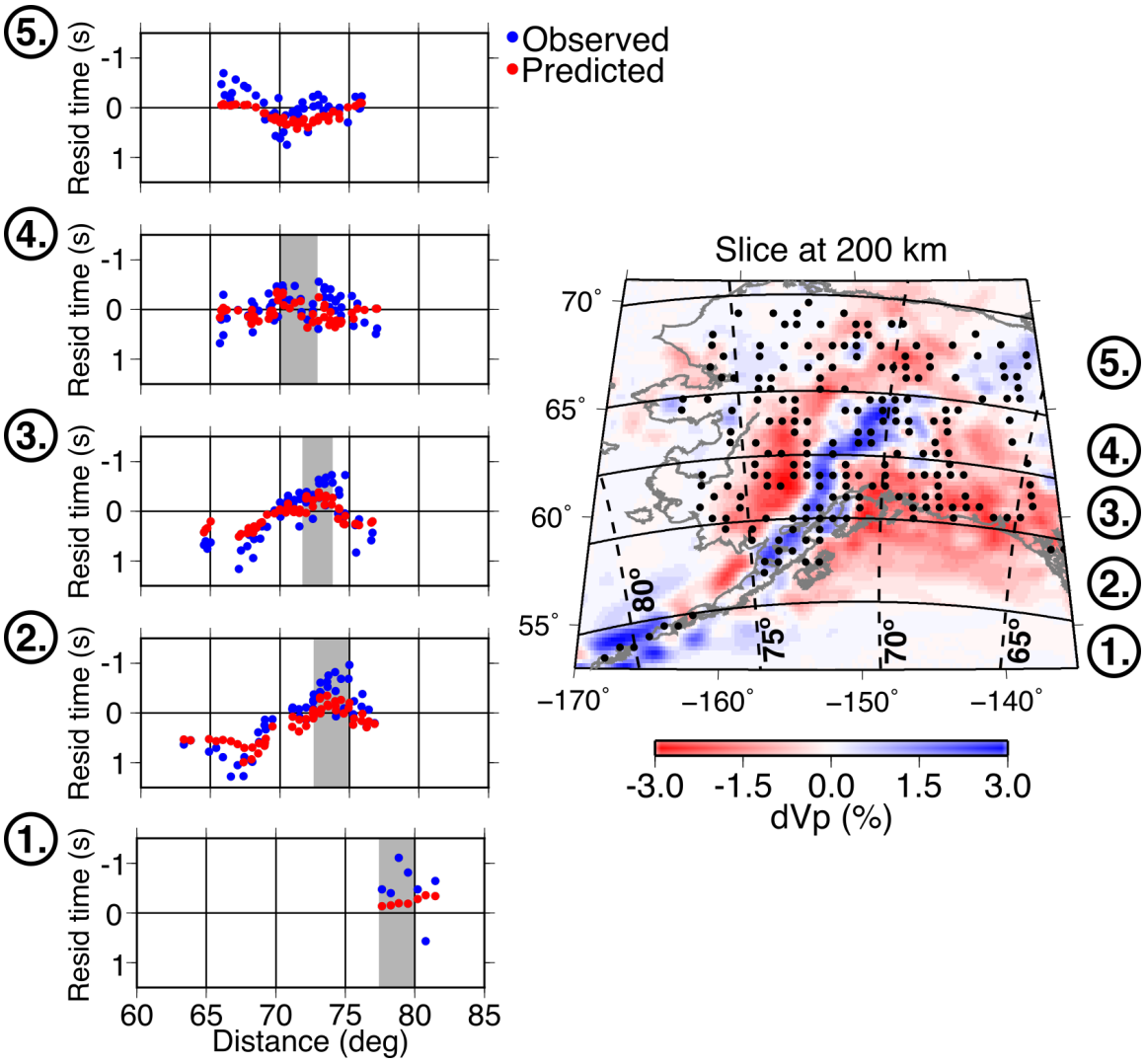

547

548 **Figure 8:** Left: Absolute P wave travel time anomalies as a function of distance and
549 for different sections through the slab for all three P wave events (Supplementary
550 Table 3), averaged together. Observations (blue) and predictions (red) from 3D ray-
551 tracing through the standard tomography model (Roecker et al., 2018). The rough
552 location of the slab in each cross section is marked by grey shading. To correct for the
553 different source-receiver distances of these events, we averaged the observed and
554 predicted P wave times as a function of receiver location, and then projected the
555 averaged receiver locations relative to the average P source location. This allows for
556 comparison with the PKPdf profiles shown in Figure 4 and Supplementary Figure 6.
557 Right: The tomography model is shown at 200 km depth, with averaged stations
558 shown as black circles. Azimuths sections shown on the left are labelled on the right.

559

560 Upper mantle structure in other regions, such as the Scotia slab under the South
561 Sandwich Islands source region (Fukao et al., 2001), may also influence the observed
562 anomalies, yet is not modelled here. Measurements of PcP-P differential travel times
563 in the region around the Scotia slab show a large range of travel time anomalies
564 (Tkalčić, 2010). The range of these anomalies is of a similar magnitude to PKPdf travel
565 time anomalies observed in Alaska from the same source region, but unlike for PKPdf,
566 they are scattered and show no systematic variation. Furthermore, Romanowicz et al.
567 (2003) demonstrated that the patterns of PKP residual travel time with ξ, distance,
568 and azimuth recorded in Alaska were observed for all SSI events, regardless of
569 location. Long et al. (2018) observe that the location of the SSI event does change the
570 distance (relative to the event) at which the trend of increasing dT is observed, but
571 we find that the geographic location of the trend is the same for all events: over the
572 Alaskan slab. Thus, while mantle structure near the Scotia slab may contribute to the
573 observations in terms of additional scatter, it is unlikely to be the cause of the
574 systematic pattern of PKPdf anomalies observed in Alaska. Moreover, the range of
575 source locations and depths used in this study would likely reduce any systematic
576 bias in our observations that would result from the Scotia slab.

577

578 The travel time of PKPdf is known to be affected by anisotropy in the inner core
579 (Supplementary Figure 1), thus we add a correction to the observed travel times. The
580 model of inner core anisotropy used is derived from data sampling the same depth
581 range and in the same hemisphere of the inner core as the South Sandwich Islands to

582 Alaska data. The strength of this correction affects the travel time anomaly that we
583 ultimately attribute to the upper mantle. Since the travel time anomaly from the inner
584 core does depend on station location this does affect the moveout of the PKPdf wave
585 across each sub array, but the effect is negligible given the small size of the sub arrays.
586 However, the correction significantly improves the match between the observed and
587 predicted travel time anomalies (Supplementary Figure 8).
588
589 As recently suggested by Long et al. (2018) and mentioned earlier, lower mantle
590 heterogeneity could influence PKP travel time anomalies. However, we calculate that
591 the magnitude of lower mantle heterogeneity that would also be compatible with
592 other observations of D'' structure, in particular PcP-P travel times (Ventosa and
593 Romanowicz, 2015), would contribute travel time anomalies on the order of no more
594 than ~1s. Core-Mantle Boundary structure instead might contribute to measurement
595 scatter or the event-specific shift from the predicted times (listed in last column of
596 Supplementary Table 1). Alternatively, the event-specific shift may result from source
597 location and origin time errors. Moreover, our upper mantle model reproduces the
598 pattern of travel time anomalies with distance from the events in the South Sandwich
599 Islands (Supplementary Figure 4). The fit is more satisfactory than that achieved by
600 Long et al. (2018) using lower mantle heterogeneity, and is also capable of explaining
601 the change in pattern with back-azimuth (Supplementary Figure 3). Furthermore, the
602 upper mantle model is capable of reproducing the patterns of slowness and back-
603 azimuth anomalies. Contamination of PKP waves by upper mantle heterogeneity thus

provides a single, self-contained explanation for patterns previously attributed to the lower mantle, outer core, and or inner core.

Conclusion

We find that the pattern of slowness, back-azimuth, and travel time anomalies measured for PKPdf at sub-arrays of the USArray in Alaska match the patterns predicted by a high-resolution model of the Alaskan upper mantle. The strong similarity of the observed slowness and back-azimuths to those predicted using only upper mantle heterogeneity suggests that it is the main source of the anomalies. This is also confirmed by analysis of direct P waves along azimuths similar to the SSI to Alaska PKP paths considered here. While other structure in the lower mantle and upper mantle on the source side may also contribute to the observed scatter in travel time residuals, we conclude that the dominant cause of the SSI-Alaskan anomaly is the Alaskan subduction zone. As such, this motivates further improvements in characterizing the structure of the Alaska slab and its surroundings. More generally, care must be taken when interpreting travel time anomalies from regions with strong upper mantle structure in terms of inner core structure.

Acknowledgements

We thank the International Seismological Centre (ISC) for access to the EHB and On-line Bulletins, http://www.isc.ac.uk, Internatl. Seismol. Cent., Thatcham, United Kingdom, 2015. The facilities of IRIS Data Services, and specifically the IRIS Data Management Center, were used for access to waveforms, related metadata, and/or

627 derived products used in this study. IRIS Data Services are funded through the
628 Seismological Facilities for the Advancement of Geoscience and EarthScope (SAGE)
629 Proposal of the National Science Foundation under Cooperative Agreement EAR-
630 1261681. Waveform simulations were performed using The Extreme Science and
631 Engineering Discovery Environment (XSEDE) supported by grants TG-EAR180020
632 and TG-EAR170001. This work was supported by EAR-1135452 and NSF grant EAR-
633 1829283.

634

635 **References**

636 Bréger, L., Tkalčić, H., Romanowicz, B.A., 2000. The effect of D'' on PKP(AB-DF)
637 travel time residuals and possible implications for inner core structure. Earth
638 Planet. Sci. Lett. 175, 133–143. https://doi.org/10.1016/S0012-
639 821X(99)00286-1
640 Cao, A., Romanowicz, B., 2007. Test of the innermost inner core models using
641 broadband PKIKP travel time residuals. Geophys. Res. Lett. 34, 1–5.
642 https://doi.org/10.1029/2007GL029384
643 Comte, D., Carrizo, D., Roecker, S., Ortega-Culaciati, F., Peyrat, S., 2016. Three-
644 dimensional elastic wave speeds in the northern Chile subduction zone:
645 Variations in hydration in the supraslab mantle. Geophys. J. Int. 207, 1080–
646 1105. https://doi.org/10.1093/gji/ggw318
647 Creager, K.C., 1999. Large-scale variations in inner core anisotropy. J. Geophys. Res.
648 104, 23127–23139. https://doi.org/10.1029/1999jb900162
649 Davies, D., Kelly, E.J., Filson, J.R., 1971. Vespa Process for Analysis of Seismic Signals.

650 Nat. Phys. Sci. 232, 8–13. https://doi.org/10.1038/physci232008a0
651 Durand, S., Thomas, C., Jackson, J.M., 2018. Constraints on D″ beneath the North
652 Atlantic region from P and S traveltimes and amplitudes. Geophys. J. Int. 216,
653 1132–1144. https://doi.org/10.1093/gji/ggy476
654 Frost, D.A., Romanowicz, B., 2019. On the orientation of the fast and slow directions
655 of anisotropy in the deep inner core. Phys. Earth Planet. Inter. 286, 101–110.
656 https://doi.org/10.1016/j.pepi.2018.11.006
657 Frost, D.A., Romanowicz, B., 2017. Constraints on Inner Core Anisotropy Using Array
658 Observations of P′P′. Geophys. Res. Lett. 44, 10,878-10,886.
659 https://doi.org/10.1002/2017GL075049
660 Frost, D.A., Rost, S., Selby, N.D., Stuart, G.W., 2013. Detection of a tall ridge at the
661 core-mantle boundary from scattered PKP energy. Geophys. J. Int. 195.
662 https://doi.org/10.1093/gji/ggt242
663 Fukao, Y., Obayashi, M., 2013. Subducted slabs stagnant above, penetrating through,
664 and trapped below the 660 km discontinuity. J. Geophys. Res. 118, 5920–5938.
665 https://doi.org/10.1002/2013JB010466
666 Fukao, Y., Widiyantoro, S., Obayashi, M., 2001. Stagnant slabs in the upper and lower
667 mantle transition region 291–323.
668 Garcia, R., Tkalčić, H., Chevrot, S., 2006. A new global PKP data set to study Earth's
669 core and deep mantle. Phys. Earth planet. Int. 159, 15–31.
670 https://doi.org/10.1016/j.pepi.2006.05.003
671 Helffrich, G., Sacks, S., 1994. Scatter and bias in differential PKP travel times and
672 implications for mantle and core phenomena. Geophys. Res. Lett. 21, 2167–

673 2170. https://doi.org/10.1029/94GL01876
674 Irving, J.C.E., Deuss, A., 2011. Hemispherical structure in inner core velocity
675 anisotropy. J. Geophys. Res. 116, 1–17. https://doi.org/10.1029/2010JB007942
676 Ishii, M., Dziewonski, A.M., 2002. The innermost inner core of the earth: Evidence for
677 a change in anisotropic behavior at the radius of about 300 km. Proc. Nat. Acad.
678 Sci. USA 99, 14026–14030. https://doi.org/10.1073/pnas.172508499
679 Jiang, C., Schmandt, B., Ward, K.M., Lin, F.C., Worthington, L.L., 2018. Upper Mantle
680 Seismic Structure of Alaska From Rayleigh and S Wave Tomography. Geophys.
681 Res. Lett. 45, 10,350-10,359. https://doi.org/10.1029/2018GL079406
682 Kennett, B.L.N., Engdahl, E.R., Buland, R., 1995. Constraints on seismic velocities in
683 the Earth from traveltimes. Geophys. J. Int. 122, 108–124.
684 https://doi.org/10.1111/j.1365-246X.1995.tb03540.x
685 Kennett, B.L.N., Gudmundsson, O., 1996. Ellipticity corrections for seismic phases.
686 Geophys. J. Int. 127, 40–48. https://doi.org/10.1111/j.1365-
687 246X.1996.tb01533.x
688 Leykam, D., Tkalčić, H., Reading, A.M., 2010. Core structure re-examined using new
689 teleseismic data recorded in Antarctica: Evidence for, at most, weak cylindrical
690 seismic anisotropy in the inner core. Geophys. J. Int. 180, 1329–1343.
691 https://doi.org/10.1111/j.1365-246X.2010.04488.x
692 Li, X., Cormier, V.F., 2002. Frequency-dependent seismic attenuation in the inner
693 core, 1. A viscoelastic interpretation. J. Geophys. Res. 107, ESE 13-1-ESE 13-20.
694 https://doi.org/10.1029/2002JB001795
695 Long, X., Kawakatsu, H., Takeuchi, N., 2018. A Sharp Structural Boundary in

696 Lowermost Mantle Beneath Alaska Detected by Core Phase Differential Travel
697 Times for the Anomalous South Sandwich Islands to Alaska Path. Geophys. Res.
698 Lett. 45, 176–184. https://doi.org/10.1002/2017GL075685
699 Lythgoe, K.H., Deuss, A., Rudge, J.F., Neufeld, J.A., 2014. Earth's inner core: Innermost
700 inner core or hemispherical variations? Earth Planet. Sci. Lett. 385, 181–189.
701 https://doi.org/10.1016/j.epsl.2013.10.049
702 Martin-Short, R., Allen, R., Bastow, I.D., Porritt, R.W., Miller, M.S., 2018. Seismic
703 Imaging of the Alaska Subduction Zone: Implications for Slab Geometry and
704 Volcanism. Geochem. Geophys. Geosyst. 19, 4541–4560.
705 https://doi.org/10.1029/2018GC007962
706 Martin-Short, R., Allen, R.M., Bastow, I.D., 2016. Subduction geometry beneath south
707 central Alaska and its relationship to volcanism. Geophys. Res. Lett. 43, 9509–
708 9517. https://doi.org/10.1002/2016GL070580
709 Miller, M.S., O'Driscoll, L.J., Porritt, R.W., Roeske, S.M., 2018. Multiscale crustal
710 architecture of Alaska inferred from P receiver functions. Lithosphere 267–278.
711 https://doi.org/10.1130/l701.1
712 Morelli, A., Dziewonski, A.M., Woodhouse, J.H., 1986. Anisotropy of the inner core
713 inferred from PKIKP travel times. Geophys. Res. Lett. 13, 1545–1548.
714 https://doi.org/10.1029/GL013i013p01545
715 Nissen-Meyer, T., Van Driel, M., Stähler, S.C., Hosseini, K., Hempel, S., Auer, L.,
716 Colombi, A., Fournier, A., 2014. AxiSEM: Broadband 3-D seismic wavefields in
717 axisymmetric media. Solid Earth 5, 425–445. https://doi.org/10.5194/se-5-
718 425-2014

719 Plafker, G., Moore, J.C., Winkler, G.R., 1994. Geology of the southern Alaska margin,
720 The Geology of Alaska. https://doi.org/10.1130/dnag-gna-g1.389
721 Rawlinson, N., Kennett, B.L.N., 2004. Rapid estimation of relative and absolute delay
722 times across a network by adaptive stacking. Geophys. J. Int. 157, 332–340.
723 https://doi.org/10.1111/j.1365-246X.2004.02188.x
724 Roecker, S., Baker, B., McLaughlin, J., 2010. A finite-difference algorithm for full
725 waveform teleseismic tomography. Geophys. J. Int. 181, 1017–1040.
726 https://doi.org/10.1111/j.1365-246X.2010.04553.x
727 Roecker, S. W., D. A. Frost, and B. A Romanowicz, Structure of the Crust and Upper
728 Mantle beneath Alaska Determined from the Joint Inversion of Arrival Times
729 and Waveforms of Regional and Teleseismic Body Waves, American
730 Geophysical Union, Fall Meeting 2018, abstract #S31C-0518.
731 Romanowicz, B., Bréger, L., 2000. Anomalous splitting of free oscillations: A
732 reevaluation of possible interpretations. J. Geophys. Res. 105, 21559–21578.
733 https://doi.org/10.1029/2000jb900144
734 Romanowicz, B., Cao, A., Godwal, B., Wenk, R., Ventosa, S., Jeanloz, R., 2015. Seismic
735 anisotropy in the Earth's innermost inner core: testing structural models
736 against mineral physics predictions. Geophys. Res. Lett. 93–100.
737 https://doi.org/10.1002/2015GL066734
738 Romanowicz, B., Tkalčić, H., Bréger, L., 2003. On the Origin of Complexity in PKP
739 Travel Time Data. Earth's Core Dyn. Struct. Rotat. 31–44.
740 https://doi.org/10.1029/GD031p0031
741 Scholl, D.W., Vallier, T.L., Stevenson, A.J., 1986. Terrane accretion, production, and

742 continental growth: a perspective based on the origin and tectonic fate of the
743 Aleutian- Bering Sea region. Geology 14, 43–47. https://doi.org/10.1130/0091-
744 7613(1986)14<43:TAPACG>2.0.CO;2
745 Selby, N.D., 2008. Application of a generalized F detector at a seismometer array.
746 Bull. Seism. Soc. Am. 98, 2469–2481. https://doi.org/10.1785/0120070282
747 Shearer, P.M., 1994. Constraints on inner core anisotropy from PKP(DF) travel
748 times. J. Geophys. Res. Solid Earth 99, 19647–19659.
749 https://doi.org/10.1029/94jb01470
750 Simmons, N.A., Myers, S.C., Johannesson, G., 2011. Global-scale P wave tomography
751 optimized for prediction of teleseismic and regional travel times for Middle
752 East events: 2. Tomographic inversion. J. Geophys. Res. 116, 1–31.
753 https://doi.org/10.1029/2010JB007969
754 Simmons, N.A., Myers, S.C., Johannesson, G., Matzel, E., 2012. LLNL-G3Dv3: Global P
755 wave tomography model for improved regional and teleseismic travel time
756 prediction. J. Geophys. Res. 117. https://doi.org/10.1029/2012JB009525
757 Song, X., 1997. Anisotropy of the Earth's inner core. Rev. Geophys. 297–313.
758 https://doi.org/10.1029/93JB0340310.1029/9
759 Souriau, A., Romanowicz, B., 1997. Anisotropy in the inner core: Relation between P-
760 velocity and attenuation. Phys. Earth planet. Int. 101, 33–47.
761 https://doi.org/10.1016/S0031-9201(96)03242-6
762 Stixrude, L., Cohen, R.E., 1995. High-Pressure Elasticity of Iron and Anisotropy of
763 Earth's Inner Core. Science (80-.). 267, 1972–1975.
764 Su, W., Dziewonski, A.M., 1995. Inner core anisotropy in three dimensions. J.

765 Geophys. Res. 100, 9831–9852. https://doi.org/10.1029/95JB00746
766 Sun, D., Helmberger, D., Miller, M.S., Jackson, J.M., 2016. Major disruption of D″
767 beneath Alaska. J. Geophys. Res. 121, 3534–3556.
768 https://doi.org/10.1002/2015JB012534
769 Suzuki, Y., Kawai, K., Geller, R.J., Borgeaud, A.F.E., Konishi, K., 2016. Waveform
770 inversion for 3-D S-velocity structure of D′′ beneath the Northern Pacific:
771 Possible evidence for a remnant slab and a passive plume dr. Earth, Planets Sp.
772 68. https://doi.org/10.1186/s40623-016-0576-0
773 Tanaka, S., Hamaguchi, H., 1997. Degree one heterogeneity and hemispherical
774 variation of anisotropy in the inner core from PKP(BC)-PKP(DF) times. J.
775 Geophys. Res. 102, 2925–2938. https://doi.org/10.1029/96JB03187
776 Tkalčić, H., 2010. Large variations in travel times of mantle-sensitive seismic waves
777 from the South Sandwich Islands: Is the Earth's inner core a conglomerate of
778 anisotropic domains? Geophys. Res. Lett. 37, 1–6.
779 https://doi.org/10.1029/2010GL043841
780 Tkalčić, H., Romanowicz, B., Houy, N., 2002. Constraints on D′′ structure using PKP
781 (AB–DF), PKP (BC–DF) and PcP–P traveltime data from broad-band records.
782 Geophys. J. Int. 148, 599–616. https://doi.org/10.1046/j.1365-
783 246X.2002.01603.x
784 Tkalčić, H., Young, M., Muir, J.B., Davies, D.R., Mattesini, M., 2015. Strong, Multi-Scale
785 Heterogeneity in Earth's Lowermost Mantle. Sci. Rep. 5, 1–8.
786 https://doi.org/10.1038/srep18416
787 Ventosa, S., Romanowicz, B., 2015. Extraction of weak PcP phases using the slant-

stacklet transform – II: constraints on lateral variations of structure near the core–mantle boundary. Geophys. J. Int. 203, 1227–1245. https://doi.org/10.1093/gji/ggv364

Vidale, J.E., 1987. Waveform effects of a high-velocity, subducted slab. Geophys. Res. Lett. 14, 542–545. https://doi.org/10.1029/GL014i005p00542

Vinnik, L., Romanowicz, B., Bréger, L., 1994. Anisotropy in the center of the inner core. Geophys. Res. Lett. 21, 1671–1674. https://doi.org/10.1029/94GL01600

Woodhouse, J.H., Giardini, D., Li, X. -D, 1986. Evidence for inner core anisotropy from free oscillations. Geophys. Res. Lett. 13, 1549–1552. https://doi.org/10.1029/GL013i013p01549

Zhiwei, L., Roecker, S., Zhihai, L., Bin, W., Haitao, W., Schelochkov, G., Bragin, V., 2009. Tomographic image of the crust and upper mantle beneath the western Tien Shan from the MANAS broadband deployment: Possible evidence for lithospheric delamination. Tectonophysics 477, 49–57. https://doi.org/10.1016/j.tecto.2009.05.007